8-1-2023

Atomically dispersed Cu-N3 on hollow spherical carbon nitride for acetaminophen degradation: Generation of 1O2 from H2O2

Shuoyuan Tian

Yu Yin

Mengxuan Liu

Lei Shi

Shu Zhang

See next page for additional authors

10.1016/j.seppur.2023.124016

Tian, S., Yin, Y., Liu, M., Shi, L., Zhang, S., Asif, A. H., ... & Sun, H. (2023). Atomically dispersed Cu-N3 on hollow spherical carbon nitride for acetaminophen degradation: Generation of 1O2 from H2O2. Separation and Purification Technology, 318, article 124016. https://doi.org/10.1016/j.seppur.2023.124016

Separation and Purification Technology 318 (2023) 124016

Contents lists available at ScienceDirect

Separation and Purification Technology

journal homepage: www.elsevier.com/locate/seppur

Atomically dispersed Cu-N_3 on hollow spherical carbon nitride for acetaminophen degradation: Generation of $^1O_2$ from H_2O_2

Shuoyuan Tian [a], Yu Yin [a,*], Mengxuan Liu [a], Lei Shi [b], Shu Zhang [b], Abdul Hannan Asif [c], Xuan Li [a], Mengqiong Liu [a], Xiaoguang Duan [d], Shaobin Wang [d], Hongqi Sun [c,*]

[a] School of Environmental and Chemical Engineering, Jiangsu University of Science and Technology, Zhenjiang 212100, China
[b] College of Materials Science and Engineering, Nanjing Forestry University, Nanjing 210037, China
[c] School of Science, Edith Cowan University, Joondalup, WA 6027, Australia
[d] School of Chemical Engineering and Advanced Materials, The University of Adelaide, Adelaide, SA 5005, Australia

ARTICLE INFO

Keywords:
AOPs
Singlet oxygen
Single atom catalyst
Fenton-like
Carbon nitride

ABSTRACT

Discharge of recalcitrant pharmaceuticals into aquatic systems has caused severe impacts on public health and ecosystem. Advanced oxidation processes (AOPs) are effective for eliminating these refractory pollutants, for which single-atom catalysts (SACs) become the state-of-the-art materials owing to the maximized exposure of active metal sites. In this work, hollow spherical graphitic carbon nitride (*hs*CN) was fabricated to incorporate copper species to develop Fenton-like catalysts for acetaminophen (ACT) removal. Through pyrolysis of supramolecular assemblies derived from melamine-Cu complex and cyanuric acid, single atom Cu-N_3 sites were anchored on *hs*CN by N-coordination to obtain SACu-*hs*CN. In virtue of the atomically dispersed Cu-N_3 sites as well as the hollow structure of *hs*CN providing smooth channels for the interactions between single Cu atoms and reactants, the optimal 5.5SACu-*hs*CN removed 94.8% of ACT after 180 min of Fenton-like reactions, which was superior to that of 5.5AGCu-*hs*CN with aggregated Cu particles on *hs*CN (56.7% in 180 min). Moreover, 5.5SACu-*hs*CN was still active after four cycles of regeneration. The mechanism investigation demonstrated that both hydroxyl radicals (˙OH) and singlet oxygen ($^1O_2$) contributed to ACT degradation in 5.5SACu-*hs*CN/H_2O_2 system, in which non-radical $^1O_2$ played the dominant role.

1. Introduction

With the rapid development of medical technology, a large number of pharmaceuticals have been synthesized for the treatment of human diseases. Acetaminophen (ACT) is a commonly used medicine for the treatment of fever and pain, thus has been widely released into water bodies and may increase the risk of kidney cancer and asthma to humans and damage the ecological environment [1,2]. In response to its water pollution, a variety of methods have been developed to alleviate the issues. Conventional strategies include adsorption [3,4], biological degradation [5,6], and advanced oxidation processes (AOPs) [7,8]. AOPs, especially Fenton-like process, are widely employed because of the advantages of strong oxidation capacity, high selectivity and easy operation [9,10]. In most Fenton-like reactions, H_2O_2 is activated to generate highly reactive hydroxyl radicals (˙OH), which carry out redox reactions to degrade organic pollutants to low-toxic intermediates, which eventually are converted to CO_2 and H_2O [11,12]. In heterogeneous metal-based Fenton-like catalysis, the interaction of H_2O_2 with metal species is the first step to initiate the Fenton-like reactions. However, as a result of the poor dispersion and aggregation of metal species, most of the interior sites of the metal species are inaccessible and have few chances to participate the reactions, therefore the activity of the catalysis is always limited. As a consequence, exploration of effective strategies to avoid metal aggregation shows a great potential for boosting the metal-based Fenton-like reactions.

Single atom catalysts (SACs) have become one of the hottest candidates for heterogeneous catalysis owing to the maximized degree of metal dispersion, 100% atomic utilization, high selectivity and activity brought about by the unsaturated coordination and unique electronic structure [13,14]. The ingredient and coordination determine the electronic and geometric structure of SACs, which have a great impact on the catalytic performances [15,16]. There have been some successful reports on SACs for AOP applications [17,18]. For instance, by pyrolyzing iron precursor and SBA-15 containing template, Yin et al. obtained the

* Corresponding authors.
E-mail addresses: season_july@just.edu.cn (Y. Yin), h.sun@ecu.edu.au (H. Sun).

https://doi.org/10.1016/j.seppur.2023.124016
Received 18 March 2023; Received in revised form 20 April 2023; Accepted 2 May 2023
Available online 4 May 2023

single atom Fe-O_4 sites in the nanopores of SBA-15 (SAFe-SBA). SAFe-SBA showed much better catalytic activity than the aggregated Fe catalyst of AGFe-SBA on H_2O_2 activation for *p*-hydroxybenzoic acid and phenol removal [19]. Li et al. anchored single atom Co sites on porous nitrogen-doped graphene to achieve a dual-sites of CoN_4. With Co for activation of peroxymonosulfate (PMS) and pyrrolic nitrogen for adsorption of organic molecules, highly effective elimination of bisphenol A within 4 min was realized [20]. Zou et al. introduced phosphorus into the Co based SACs to implement a unique CoN_3P site, and the prepared ZIF-CoN_3P-C catalyst showed a remarkable catalytic performance, degrading 98.4% of sulfadiazine in 5 min [21]. Wang et al. designed N-doped graphene-supported single copper atom catalyst of Cu_1/NG, which achieved ultrafast removal of bisphenol A within 5 min [22]. Indeed, SACs can achieve fascinating catalytic performances, and have attracted ever-growing attention for AOP towards the degradation of water contaminants.

Graphitic carbon nitride (g-C_3N_4) has received tremendous interests by virtues of metal-free, low cost, nitrogen-rich, environmental-friendly properties, and versatile applications [23,24]. The high density and uniform nitrogen atoms in its matrix as well as the six-fold cavities provide a favorable environment for capturing and interacting with transition metal atoms at the interface [25,26]. In recent years, g-C_3N_4 has been widely manufactured with a sheet-like morphology to host metal species for water treatment by non-photocatalytic AOPs [27,28]. It is important to highlight that some metal sites have reached the atomic dispersion level. Zhang et al. developed lamellar g-C_3N_4 supported Fe single atoms (Fe_1/CN), which rapidly degraded 100% of p-chlorophenol, 2,4-dichorophenol, bisphenol and sulfamethoxazole within 10 min by activation of PMS [29]. Duan et al. used multilayered g-C_3N_4 to fabricate a single atom Fe catalyst of SAFe-CN, and its filter under PMS activation could degrade 100% of o-phenylphenol after 100 h of dynamic and continuous operation [30]. Guo et al. anchored single Mn atoms on multi-layered g-C_3N_4 to prepare SAC of Mn-CN, and complete removal of oxalic acid was finished within 40 min by adding O_3 and H_2O_2 [31]. In addition to the layered architecture, g-C_3N_4 has also been fabricated with tubular [32,33], spherical [34,35], ribbony [36,37] and fibered [38,39] nanostructures. However, they are commonly used in photocatalysis, and rarely studied in the non-photocatalytic AOP applications. In particular, the spherical g-C_3N_4 with a unique hollow nanostructure can provide rich voids and large specific surface areas. Moreover, the hollow loose structure endows the connected metals with high accessibility to reactants, which are favorable for the catalyst to serve as the oxidant stimulator in AOPs.

Unlike the critical demand of acid environment in conventional Fenton reactions, copper based catalysts are well-known to be effective to activate H_2O_2 over a broad working pH range. Herein, for the first time, single atom Cu was anchored on hollow spherical g-C_3N_4 (*hs*CN) for Fenton-like reactions. Melamine-Cu complex was preassembled with cyanuric acid in the DMSO solution, and after thermal polymerization, the resulting SACu-*hs*CN was achieved (Scheme 1). The hollow spherical structure of SACu-*hs*CN was well characterized by SEM, HRTEM and BET. The precise formation of single atom Cu in 5.5SACu-*hs*CN was well determined by aberration corrected (AC) HAADF-STEM and EXAFS techniques. The SAC of 5.5SACu-*hs*CN as a H_2O_2 activator could degrade 94.8% of ACT after 180 min of Fenton-like reactions. This performance outperformed 5.5AGCu-*hs*CN with aggregated Cu particles on *hs*CN (56.7% in 180 min). The investigation on the correlation of intrinsic structure-performance demonstrated that the higher activity on H_2O_2 stimulation and ACT removal was contributted to the atomic level of Cu-N_3 sites in 5.5SACu-*hs*CN with the hollow spherical structure. The results of EPR and quenching tests revealed that besides •OH radicals, non-radical of $^1O_2$ was also produced in the 5.5SACu-*hs*CN/H_2O_2 system. Moreover, $^1O_2$ predominantly worked for the decontamination of ACT. This work provides new insights for the design and synthesis of atomically dispersed heterogeneous metal-based AOP catalysts for pollutant elimination.

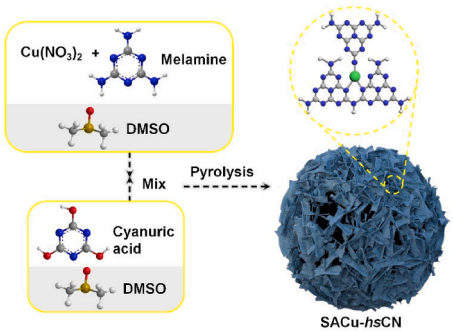

Scheme 1. Synthesis route of the SACu-*hs*CN catalyst.

2. Experimental section

2.1. Synthesis of hsCN

The information of chemicals and reagents is given in the supporting text (Text S1). The material of *hs*CN was fabricated according to the reported approach with some modifications [35]. The 0.5 g of melamine and 0.51 g of cyanuric acid were firstly dissolved in 20 mL of DMSO by ultrasound respectively, and then the DMSO solution of cyanuric acid was slowly dropped into the DMSO solution of melamine. After stirring for 10 min, the solution was filtered, washed and dried to obtain the supramolecular polymers of melamine and cyanuric acid, namely *hs*CN precursor. Finally, the precursor powder was calcined at 550 °C for 4 h in the atmosphere of high purity nitrogen to obtain the resultant *hs*CN.

2.2. Synthesis of SACu-hsCN

The material of SACu-*hs*CN was synthesized by the following procedures. To start, a certain amount of $Cu(NO_3)_2{\cdot}3H_2O$ and 0.5 g of melamine were dissolved in 20 mL of DMSO and the green transparent solution was then obtained after ultrasound for 10 min. In another beaker, 0.51 g of cyanuric acid was fully dissolved in 10 mL of DMSO by ultrasound for 10 min. Then above two solutions were mixed, and magnetically stirred for 10 min. The color of solution changed from green to blue, and finally white green turbidity was formed. After filtration, the light green powder was obtained by washing with 150 mL of deionized water and 100 mL of anhydrous ethanol, and then the powder was dried in the oven at 60 °C for 12 h. Finally, the powder was calcined at 550 °C in a high purity nitrogen atmosphere at a rate of 2.3 °C·min^{-1} for 4 h. The resulting yellow–brown sample was designated as SACu-*hs*CN.

2.3. Synthesis of AGCu-hsCN

The material of AGCu-*hs*CN was prepared by the classical impregnation method. Firstly, the *hs*CN precursor was synthesized following the procedure as described above. Then, the *hs*CN precursor and Cu $(NO_3)_2$ $3H_2O$ were fully dissolved in 10 mL of deionized water, and evaporated to dry in a 50 °C ambient water bath. After that, the acquired powder was calcined at 550 °C for 4 h in a tube furnace at a rate of 2.3 °C·min^{-1} under high purity nitrogen atmosphere. The target sample of AGCu-*hs*CN was obtained.

The weight content (wt%) of Cu in SACu-*hs*CN and AGCu-*hs*CN was regulated by changing the initial dosage of $Cu(NO_3)_2{\bullet}3H_2O$, and monitored by ICP-OES and labelled as a prefix number before SACu-*hs*CN and AGCu-*hs*CN, respectively.

2.4. Catalytic oxidation

The properties of the catalysts were characterized with the details

provided in Text S2. Catalytic oxidation and analysis were depicted as follows. The catalytic oxidation was carried out in a 500 mL of beaker under continuous agitation. If no specific description, the temperature was controlled at 40 °C by a water bath. The volume of the target ACT solution was 250 mL with the concentration of 20 mg·L^{-1}, and the dosage of catalyst and H_2O_2 was 0.2 g·L^{-1} and 1000 ppm respectively. While testing the effect of pH on the degradation, the solution of 0.2 M KOH and 0.2 M H_2SO_4 was separately added to adjust the pH value. To start the reaction, the catalyst was firstly added into the target ACT solution and stirred for 30 min to reach adsorption–desorption equilibrium. After that, with the addition of H_2O_2, the Fenton-like oxidation was initiated. During the predetermined intervals, 1 mL of the reaction solution was extracted with a syringe, filtered by 0.22 μm membrane, and quenched with 0.5 mL of methanol to suspend the oxidation. Finally, the concentration of residual ACT was analyzed by a high performance liquid chromatography (HPLC) on the model of LC-20 CE from Shimadzu. The mobile phase consisted of water and methanol at the ratio of 35:65 and was at the flow rate 0.5 mL·min^{-1}. The chromatographic column was Agilent 5 TC-C18 (250 × 4.6 mm). The ACT pollutant was separated from the mixture with the column temperature at 30 °C and tested by the ultraviolet detector at the wavelength of 244 nm. The rate constant of *k* for the Fenton-like reactions was calculated on the basis of the first order kinetic theory in Eq. (1). In the formula, c_0 and c were the ACT concentrations at the initial time and time t, respectively.

$$ln\left(\frac{c_0}{c}\right) = kt \quad (1)$$

3. Results and discussion

3.1. Characterization of hsCN and Cu containing samples

XRD patterns of *hs*CN and Cu containing samples are shown in Fig. 1a-b. The pristine *hs*CN has two diffraction peaks at 13° and 27.4°, corresponding to (1 0 0) and (0 0 2) crystal planes of g-C_3N_4, respectively [40]. With the incorporation of Cu, the peak at 13° disappears, indicating that the growing of graphitic layer in large dimensions is prevented. The peak at 27.4° slightly shifts to a low angle of 26.8°, and significantly decreases in intensity. This elucidates that the introduction of Cu expands the interlayer distance of g-C_3N_4, leads to that the structure becomes looser, and distorts the graphitic structure. Nevertheless, the basal structure of g-C_3N_4 matrix is maintained after Cu loading. Remarkably, three sharp diffraction peaks at 43.3°, 50.4°, and 74.1° newly emerge on 5.5AGCu-*hs*CN, assigning to Cu (1 1 1), Cu (2 0 0), and Cu (2 2 0), which are in accordance with the Cu standard card (PDF no. 04–0836). The formation of aggregated Cu particles on g-C_3N_4 is thus deduced, and the particle size is about 23.5 nm (Scherrer formula). It is worth noting that none of the redundant peak attributing to copper species can be observed on 5.5SACu-*hs*CN, while ICP-OES measurement exactly quantifies the Cu content of 5.5 wt%. This illustrates that the guest copper achieves high dispersion on g-C_3N_4 without any particle aggregation of copper species. Other SACu-*hs*CN analogues (Fig. 1b) exhibit similar XRD profiles to 5.5SACu-*hs*CN with no characteristic peaks of copper species detected. Additionally, with the increase of Cu content from 2.4 to 6.3 wt%, the peak intensity of SACu-*hs*CN at 26.8° gradually decreases, which suggests that the loading of Cu affects the crystal growth of g-C_3N_4 and results in a decline in the crystallinity of SACu-*hs*CN [41]. The XPS survey spectra are depicted in Fig. 1c. The peaks of C 1s and N 1s belonging to g-C_3N_4 are observable on *hs*CN and 5.5SACu-*hs*CN samples. In comparison with *hs*CN, two peaks contributing to Cu $2p_{3/2}$ and Cu $2p_{1/2}$ newly emerge on 5.5SACu-*hs*CN, confirming the existence of Cu despite no XRD signals. On the Cu 2p XPS core-level spectrum of 5.5SACu-*hs*CN (Fig. 1d), the peaks located at 931.5 and 952.1 eV are identified to be Cu $2p^{+}_{3/2}$ and Cu $2p^{+}_{1/2}$, respectively. No Cu(II) satellite peak appears in the region of 940–950 eV, confirming that Cu is probably at the oxidation state of + 1 [42].

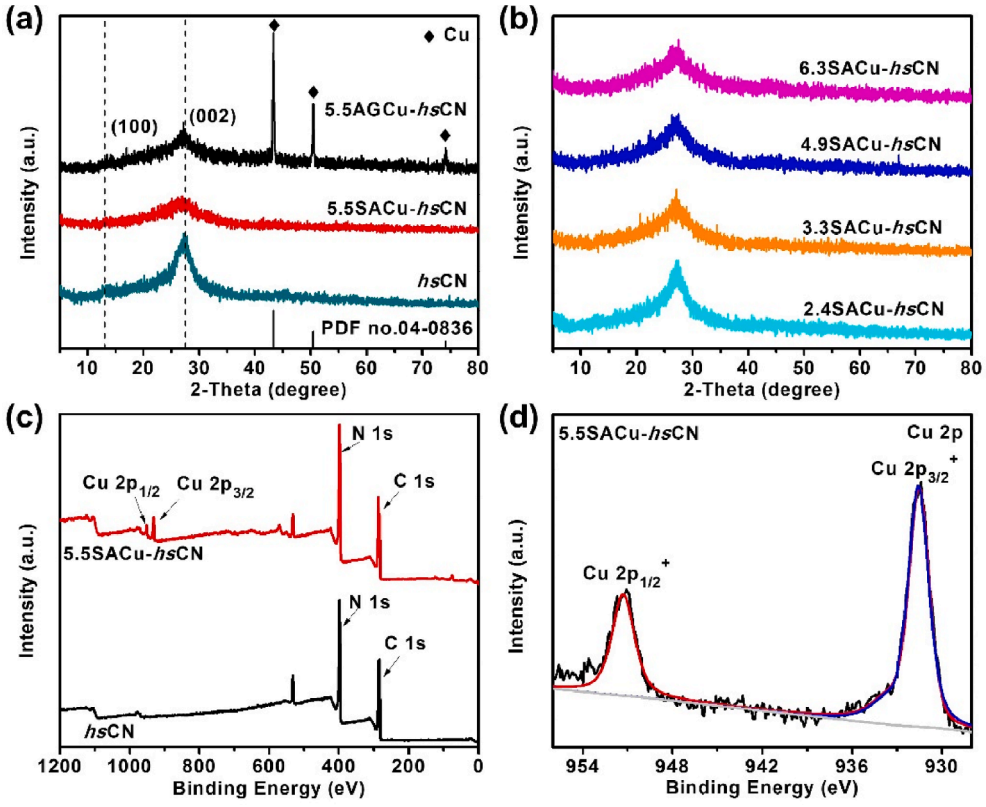

Fig. 1. XRD patterns of (a) *hs*CN, 5.5SACu-*hs*CN, 5.5AGCu-*hs*CN, and (b) SACu-*hs*CN analogues; (c) XPS survey spectra of *hs*CN and 5.5SACu-*hs*CN; (d) Cu 2p XPS core-level spectrum of 5.5SACu-*hs*CN.

The detailed surface chemical compositions of *hs*CN and 5.5SACu-*hs*CN are characterized by XPS. In high-resolution C 1s spectra (Fig. 2a and c), peaks at 284.6, 286.0 and 288.1 eV are attributed to sp^2 hybrid amorphous carbon (C—C), C—NH_2 at the edge of heptazine unit, and carbon atoms (N—C═N) on the triazine ring of g-C_3N_4, respectively [43,44]. The broad XPS peak of N 1s for *hs*CN can be deconvoluted into four peaks as profiled in Fig. 2b. The combined peaks of 398.3, 399.2, 400.4 and 404.1 eV are assigned to the sp^2 C═N—C bonds in the tri-s-triazine (pyridinic N), sp^3 tertiary nitrogen N—$(C)_3$ groups (pyrrolic N), N—H groups (graphitic N) and oxidized N, respectively [45,46]. Compared with *hs*CN, the pyridinic N of 5.5SACu-*hs*CN shifts to a lower binding energy of 398.1 eV (Fig. 2d). Then it is rational to speculate that Cu atoms may electronically interact with pyridinic N to form Cu-N*x* coordination. Moreover, a new peak at 399.0 eV appears on the N 1s spectrum of 5.5SACu-*hs*CN in contrast to pristine *hs*CN, further implying the formation of the Cu-N*x* bonds [47,48].

SEM image of *hs*CN (Fig. S1) shows the loose spherical nanostructure, which is assembled by numerous crumpled nanosheets. The Cu loaded samples of 2.4–5.5SACu-*hs*CN display the similar spheres as *hs*CN (Figs. 3a-c and S2a-c), indicating that their morphologies are not affected by the incorporation of 2.4–5.5 wt% of Cu, in consistent with the results of XRD. A little damage is observed on the 6.3SACu-*hs*CN spheres (Fig. S2d), which illuminates that excessive Cu destroys the spherical morphology. It is noted that the spheres of both *hs*CN and SACu-*hs*CN seem like hollow. In order to investigate the interior structure, HRTEM images are presented in Fig. 3d-e. As shown, the 5.5SACu-*hs*CN sample displays spheres with an average diameter of 1–2 μm, and with the loose hollow feature. Besides, there are no aggregated particles on the enlarged HRTEM images (Fig. 3f). It is found that noticeable particles emerge on the enlarged TEM image of 5.5AGCu-*hs*CN (Fig. S3). Further HAADF-STEM image and EDX elemental mapping of 5.5SACu-*hs*CN demonstrate that C, N and Cu elements are homogeneously dispersed in the hollow spherical structure (Fig. 3g). The results of N_2 adsorption–desorption experiments disclose the type IV isotherms of *hs*CN and 5.5SACu-*hs*CN samples (Figure S4), coinciding with the loose hollow structure. The specific BET surface areas and pore volumes are 95 $m^2 \bullet g^{-1}$, 0.354 $cm^3 \bullet g^{-1}$ for *hs*CN and 75 $m^2 \bullet g^{-1}$, 0.390 $cm^3 \bullet g^{-1}$ for 5.5SACu-*hs*CN, respectively (Table S1). 5.5SACu-*hs*CN has a smaller BET surface area than the pristine *hs*CN, which may be due to the substitution of melamine by melamine-copper supramolecular polymers.

To gain more insights into the dispersion of copper species on *hs*CN, aberration corrected (AC) HAADF-STEM was further employed. As exhibited in Fig. 4a-b, single-atom-sized bright spots of Cu atoms are isolated and uniformly distributed throughout the 5.5SACu-*hs*CN. The electronic structure and coordination environment of Cu species at the atomic scale in 5.5SACu-*hs*CN were further explored by X-ray absorption spectroscopy (XAS). Fig. 4c shows the Cu K-edge XANES spectra of copper foil, copper oxide (CuO), cuprous oxide (Cu_2O), copper phthalocyanine (CuPc) and 5.5SACu-*hs*CN. The position of the Cu K-edge absorption threshold of 5.5SACu-*hs*CN is located inside the range of the Cu foil, CuO and CuPc, and coincided with Cu_2O, indicating that the oxidation state of Cu in 5.5SACu-*hs*CN is + 1, which is in agreement with the XPS results. The R-space Fourier transform (FT) EXAFS spectrum of 5.5SACu-*hs*CN (Fig. 4d) transformed from k^3-weighted χ(k) (Fig. S5) shows the single peak at about 1.5 Å, corresponding to the Cu–N coordination [49–51]. Meanwhile, no Cu-Cu coordination peak is detected at about 2.2 Å, implying the dispersion of isolated Cu atoms on the *hs*CN substrate. The wavelet transform (WT) analysis diagram is presented in Fig. 4e to observe the backscattered atoms. 5.5SACu-*hs*CN shows the largest WT center at 4.2 $Å^{-1}$, which is distinguished from those of reported reference samples of Cu—Cu in Cu foil, Cu—O in CuO and Cu—N in CuPc [52–54]. Based on the EXAFS curve fitting (Fig. 4f and Table S2), the coordination number of the central Cu atoms is about 2.7 and the average bond length was 1.94 Å, which proposes that the each Cu atom in 5.5SACu-*hs*CN is coordinated with three N atoms as Cu-N_3.

Taking the above observations into account, we carefully draw the following conclusions. (i) First of all, the architecture of hollow spherical g-C_3N_4 has been successfully constructed by pyrolysis of the supramolecular assemblies from the reaction between melamine and cyanuric acid in DMSO solution. The XRD pattern of *hs*CN indicates its g-C_3N_4 matrix. The SEM image reveals its spherical morphology with a certain open interior structure. The considerable BET surface area and pore

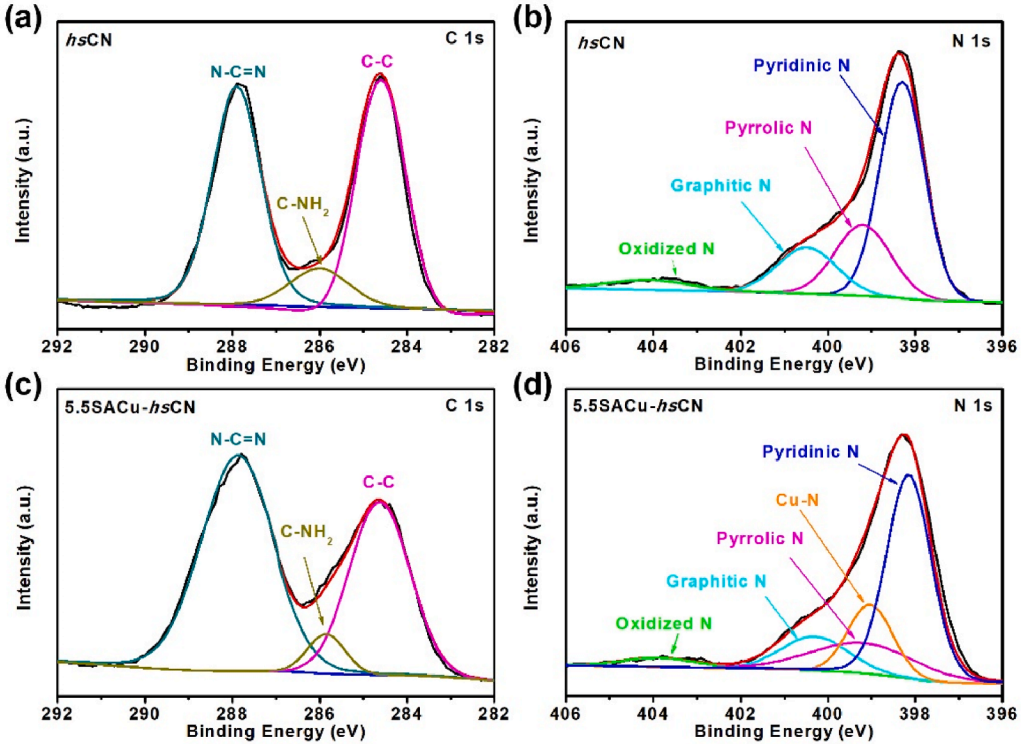

Fig. 2. XPS spectra of (a) C 1s, (b) N 1s of *hs*CN, and (c) C 1s, (d) N 1s of 5.5SACu-*hs*CN.

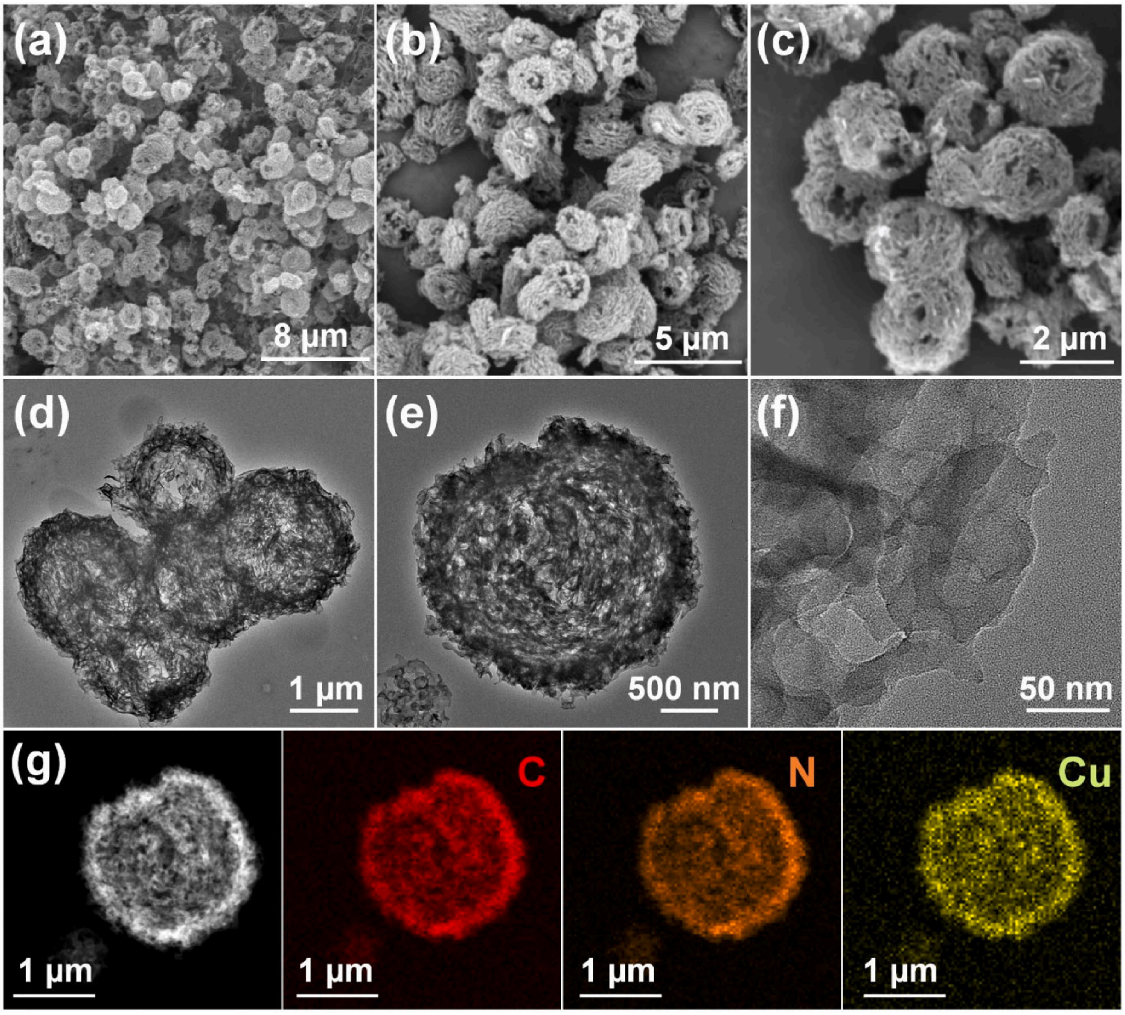

Fig. 3. (a-c) SEM images and (d-f) HRTEM images of 5.5SACu-*hs*CN; (g) EDX mapping of C, N and Cu elements.

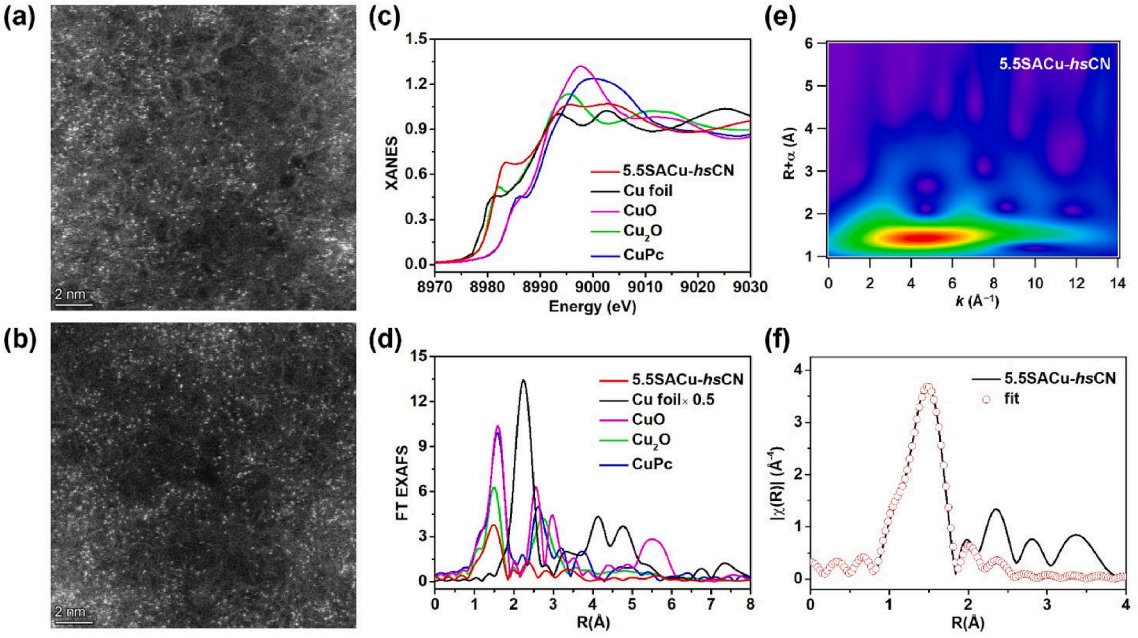

Fig. 4. (a-b) Aberration corrected HAADF-STEM image of 5.5SACu-*hs*CN; (c) the experimental Cu K-edge XANES spectra, (d) R-space FT-EXAFS spectra of 5.5SACu-*hs*CN and the reference samples; (e) WT-EXAFS plots, (f) FT-EXAFS R-space fitting curve of 5.5SACu-*hs*CN. (Reference samples: Cu foil, CuO, Cu_2O and CuPc).

volume provide circumstantial evidence for the hollow property of *hs*CN. (ii) Secondly, Cu doping is confirmed and has little effect on the structural integrity of pristine *hs*CN. As for 5.5AGCu-*hs*CN, the obvious Cu diffraction on XRD directly ascertains the Cu modification. With regard to SACu-*hs*CN, although no detection of copper species by XRD, Cu element is detected and quantified by ICP-OES. In particular, the Cu 2p peaks on XPS spectrum and the abundant Cu spots on the EDX element mapping of 5.5SACu-*hs*CN prove the existence of Cu. In addition, the characteristic peaks belonging to *hs*CN on XRD patterns of SACu-*hs*CN can still be observed. SEM images of 2.4–5.5SACu-*hs*CN exhibit the good spherical nanostructures with suspected hollow inside are maintained, however, slight distortion occurs on 6.3SACu-*hs*CN. The clear hollow core is visible on the HRTEM image of 5.5SACu-*hs*CN, which is also found to own a large BET surface area and pore volume. That is to say, hollow spherical g-C_3N_4 has no damage after Cu incorporation except for the excessive doping. (iii) Third, the guest Cu is found to achieve atomic dispersion on *hs*CN in the form of Cu-N_3. The undetectable XRD peaks concerning to copper species for Cu containing samples of SACu-*hs*CN clarify the high dispersion of Cu on *hs*CN with no particle agglomeration. When referring to 5.5SACu-*hs*CN, the uniform dispersion of Cu on *hs*CN is also described by the EDX element mapping spectra. XPS results illuminate the host–guest interaction is probably established by Cu-N*x* bonds. AC HAADF-STEM images further shed light on the precise formation of single atom Cu on *hs*CN. EXAFS profiles and curve fitting manifest no Cu-Cu bond, and the single atom Cu coordinates with three number of N atoms as Cu-N_3.

3.2. Catalytic oxidation on hsCN and Cu containing samples

ACT was chosen as the target pollutant to be oxidized in Fenton-like reactions to investigate the catalytic activities. Fig. 5a-b illustrated the results of *hs*CN and Cu containing samples. It could be clearly seen that the removal of ACT by these catalysts was almost negligible after 30 min of adsorption–desorption equilibrium. Afterwards, the oxidant of H_2O_2 was added to conduct Fenton-like reactions. H_2O_2 itself has no effect on the degradation of ACT, possibly because H_2O_2 alone is insufficient to conduct catalytic oxidation. The *hs*CN/H_2O_2 system could hardly degrade ACT as well, indicating that pristine *hs*CN was unable to activate H_2O_2 to produce reactive oxygen species. In contrast to the inactive *hs*CN, the activity of Cu containing samples was greatly improved. It was found that the activities of ACT degradation were positively correlated with the Cu content in 2.4–5.5SACu-*hs*CN catalysts. After 180 min of reaction with H_2O_2, the removal efficiency was increased from 62.5% up to 94.8% while raising the Cu amount from 2.4 wt% to 5.5 wt% for SACu-*hs*CN. When Cu content was further increased to 6.3 wt% for 6.3SACu-*hs*CN, the catalytic activity slightly declined, and 92.8% of ACT was eliminated with H_2O_2. The possible reason for the inferior activity of 6.3SACu-*hs*CN than 5.5SACu-*hs*CN was the structural distortion as stated above. The counterpart sample of 5.5AGCu-*hs*CN containing the identical Cu as the optimal 5.5SACu-*hs*CN only degraded 56.7% of ACT in 180 min of oxidation with H_2O_2. The rate constant (*k*) for the optimal 5.5SACu-*hs*CN was further calculated to be 0.035 min^{-1}, which was 3.6 times larger than that of 5.5AGCu-*hs*CN (0.0097 min^{-1}). After normalizing with the amount of Cu atoms, the *k* value was 12.7 $min^{-1}\bullet g^{-1}$ for 5.5SACu-*hs*CN, and only 3.5 $min^{-1}\bullet g^{-1}$ for 5.5AGCu-*hs*CN. The *k* value of 5.5SACu-*hs*CN was further normalized with specific BET surface area, and the result was 0.17 $min^{-1}\bullet m^{-2}$. ACT degradation performances with various materials in H_2O_2 induced Fenton-like reactions were collected in Table S3 for comparison. It can be summarized that the activity of 5.5SACu-*hs*CN surpassed not only those Cu containing catalysts of 5.5AGCu-*hs*CN, $Fe_{25}Cu_{75}$/CNT, Cu-Zn-Fe-LDH and Fe(II)/CuO, but also the Fe based catalyst of Fe-MFI and Fe_3O_4@SiO_2. It was also found that 5.5SACu-*hs*CN still showed similar activity with Fe-SBA-15 $(20)_{Fe2(SO4)3}$ and Pyrite with ultra-high dosage of catalysts, as well as Co-FeOCl with an ultra-low concentration of ACT. Although 5.5SACu-*hs*CN seemed to be inferior to Fe_3O_4@SiO_2@Cu, but the reaction condition of ultra-low ACT concentration should be noted.

The concentration of leaching Cu ions in the reaction solution of 5.5SACu-*hs*CN/H_2O_2 after 180 min of ACT degradation was measured to be 0.7 mg$\bullet L^{-1}$ by ICP-OES, which was accredited under the European Union regulation of below 2.0 mg$\bullet L^{-1}$. In order to differentiate the role of catalysis that was played by whether the heterogeneous 5.5SACu-*hs*CN or the leaching Cu ions, the content of Cu leaching after 60 min was further tested to be 0.2 mg$\bullet L^{-1}$, since up to 76.8% of ACT was degraded by 5.5SACu-*hs*CN at this time. The degradation of ACT by the Cu ions equal to 0.2 mg$\bullet L^{-1}$ was thus studied, and the result revealed only about 11.2% of ACT was removed within 60 min. Therefore, it was reasonable to conclude that the key role of the Fenton-like reactions was the heterogeneous catalyst rather than the leaching Cu ions. To this end, some findings on the relationship of structure-performance were able to be made. The pristine *hs*CN was ineffective for the activation of H_2O_2, while Cu containing samples exhibited efficient activity. Therefore, in

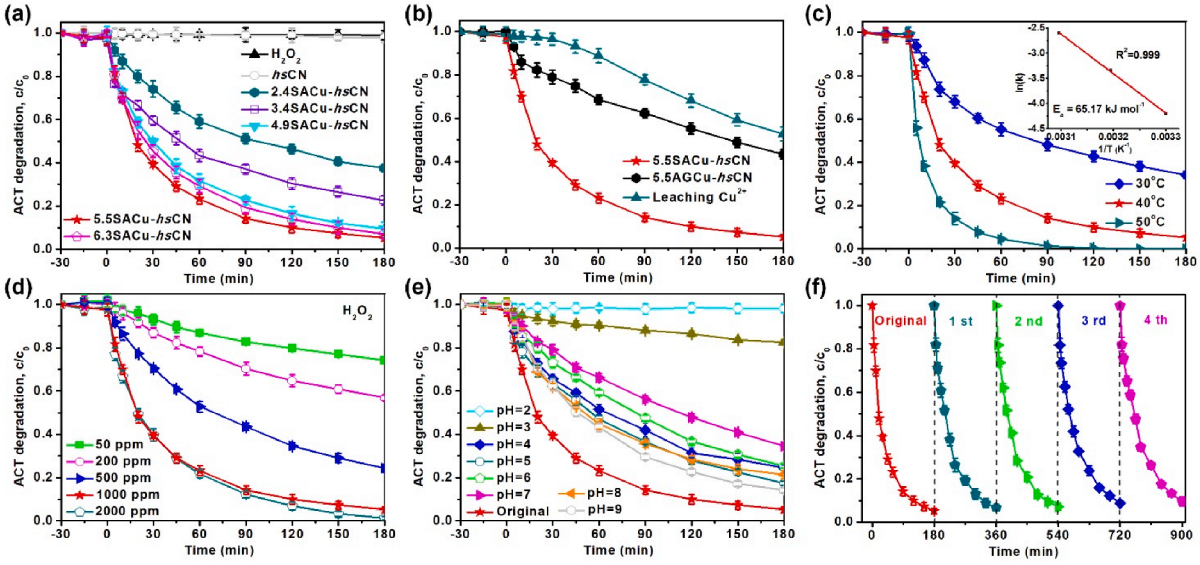

Fig. 5. (a-b) ACT adsorption and degradation by H_2O_2 activation on diverse catalysts; effects of reaction parameters on the ACT degradation for 5.5SACu-*hs*CN: (c) temperature, (d) H_2O_2 dosage, and (e) initial pH value, (f) regeneration cycles of 5.5SACu-*hs*CN for ACT degradation reaction. Except for the explored parameters, others were fixed. ($[Catalyst]_0$ = 0.2 g·L^{-1}, $[H_2O_2]_0$ = 1000 ppm, [T] = 40 °C, and $[ACT]_0$ = 20 mg·L^{-1}).

the SACu-*hs*CN and AGCu-*hs*CN catalysts, the hollow spherical g-C_3N_4 matrix had no effect on H_2O_2 stimulation, while the guest Cu afforded the responsibility. The superior activity of 5.5SACu-*hs*CN to 5.5AGCu-*hs*CN was thus deduce to be related to the different dispersion behaviors of guest Cu. The single atom Cu in 5.5SACu-*hs*CN exposed maximized active Cu sites, and the porous structure of g-C_3N_4 provided the accessible channels to reactants. Thus, the active single Cu atoms in 5.5SACu-*hs*CN could thoroughly contact then activate H_2O_2, and facilitate the significant catalytic performance on ACT elimination. However, the agglomeration of Cu in 5.5AGCu-*hs*CN gave rise to the majority of Cu species having little chance to interact with H_2O_2, which greatly inhibited the H_2O_2 activation and ACT oxidation.

The influences of reaction parameters including temperature, dosage of H_2O_2 and pH on ACT degradation for 5.5SACu-*hs*CN/H_2O_2 system were studied (Fig. 5c-e). As shown in Fig. 5c, the catalytic activity of 5.5SACu-*hs*CN/H_2O_2 was studied at different temperatures. When the temperature was set at 30 °C, 65.9% of ACT was degraded, and at 40 °C, 94.8% of ACT was eliminated in 180 min. Further increasing the temperature to 50 °C, 100% of ACT removal reached within 120 min. It was then educed that the elevated temperature was favorable for ACT degradation. At 30, 40, and 50 °C, the rate constant (*k*) was evaluated to be 0.015, 0.035 and 0.074 min^{-1}, respectively. The activation energy (E_a) for 5.5SACu-*hs*CN/H_2O_2 on the degradation of ACT was estimated to be 65.17 $KJ{\cdot}mol^{-1}$ by use of Arrhenius equation [19]. The effect of H_2O_2 dosage was explored and the results were profiled in Fig. 5d. Within 180 min, 25.8%, 43.1% and 75.7% of ACT was removed with H_2O_2 at 50, 200 and 500 ppm, respectively. The activity was quite inferior to that of 1000 ppm of H_2O_2 dosage (94.8%). When H_2O_2 concentration was added to 2000 ppm, 98.8% of ACT was degraded in 180 min. It was seen that while H_2O_2 dosage increased from 1000 to 2000 ppm, the efficiency of ACT oxidation was merely slightly improved. At the same time, when the amount of H_2O_2 was 2000 ppm, the dissolution content of Cu ions in the solution after the 180 min of reaction was 1.1 $mg{\cdot}L^{-1}$, which was much higher than 0.7 $mg{\cdot}L^{-1}$ for the 1000 ppm of H_2O_2. Therefore, 1000 ppm of H_2O_2 was determined as the optimal dosage. It was known that the changes of pH value always had a great influence on Fenton-like reactions, so it is essential to monitor the function of various pH values on the Fenton-like degradation of ACT by 5.5SACu-*hs*CN/H_2O_2. In this catalytic system, it was discovered that the pH value of the solution was nearly stable as the reaction in progress, so the initial pH value was adjusted. As presented in Fig. 5e, 94.8% ACT could be degraded in 180 min at the original solution with pH value of 5.4. When the solution was acidified to the pH value of 2 and 3, the degradation significantly decreased. At pH of 2, the catalytic reaction had almost no activity, and the removal efficiency of ACT was less than 2% after 180 min. At pH of 3, as low as 17.4% of ACT was removed after 180 min. At pH of 4, 5, 6 and 7, the passable activity of 75.4%, 82.6%, 74.6% and 65.4% of ACT were recorded in 180 min, respectively. As the pH value further promoted to the alkaline condition of 8 and 9, 78.5% and 85.8% of ACT was degraded within 180 min. The first-rank degradation activity occurred at the original reaction solution with pH value of 5.4. The wide working pH range was found for the 5.5SACu-*hs*CN/H_2O_2 system,which endowed it a huge prospect to be applied in practical water treatment.

In order to examine the reusability of 5.5SACu-*hs*CN for H_2O_2 activation and ACT degradation, the used 5.5SACu-*hs*CN was recovered by filtration, washing and drying at 60 °C. The XRD and SEM image of used 5.5SACu-*hs*CN were discovered to be similar to the fresh sample (Fig. S6). No sign of aggregation of Cu species on XRD and the integrity of hollow spherical morphology on SEM image indicated the structural stable after the Fenton-like reaction. After the first, second and third cycle, the degradation of ACT at 180 min decreased from the original of 94.8% to 85.5%, 75.7% and 74.1%, respectively (Fig. S7). The activity of 5.5SACu-*hs*CN slightly declined after repeated uses for three times, but was still satisfactory. The slight reduction of activity was possibly resulted from two issues: (i) the feeble reduction of Cu content in the catalyst caused by the leaching of metal during the previous oxidation process, and (ii) the cover of the active metal sites stemmed from the attachment of intermediates and oxygen-containing groups to the catalyst surface. Thermal treatment was commonly used to desorb the intermediates and remove oxygen-containing groups on the catalyst to promote the recovery of the original structure. After annealed at 550 °C for 1 h in high purity nitrogen, the regenerated 5.5SACu-*hs*CN removed 93.3%, 92.8%, 91.3%, and 90.3% of ACT respectively for the four regeneration cycles (Fig. 5f). The regenerated 5.5SACu-*hs*CN restored high catalytic activity, and similar performance as the fresh catalyst was revealed. Overall, the 5.5SACu-*hs*CN/H_2O_2 system provided a good durability, which was highly desired in practical water treatment.

3.3. Identification of reactive oxygen species

The reactive oxygen species (ROSs) in Fenton-like reactions on ACT degradation were identified by direct and indirect methods. Electron paramagnetic resonance (EPR) tests were conducted to directly identify the produced ROSs. As can be seen in Fig. 6a, by using DMPO as the trapping agent, a four-peak signal with the intensity ratio of the quartet 1:2:2:1 can be observed, suggesting the formation of DMPO-$^{\bullet}$OH [55]. When TEMP was used as a collector, the 1:1:1 triplet-peak signal of TEMP-$^1O_2$ was detected [27]. Both the signal intensities of DMPO-$^{\bullet}$OH and TEMP-$^1O_2$ became stronger with the prolonged reaction time from 1 to 10 min. The radicals of $^{\bullet}$OH and $^1O_2$ were also detectable in the 5.5AGCu-*hs*CN activated H_2O_2 system (Fig. S8). In the indirect means, quenching experiments by use of different scavengers were carried out. Tert-butanol (TBA) was well established as an effective quenching agent for hydroxyl radical ($^{\bullet}$OH), and L-histidine was commonly reported as a suitable quencher for singlet oxygen ($^1O_2$) [56,57]. The rate constants between ROSs and scavengers were listed in Table S4, and scavengers were found to have no reaction with H_2O_2 (Fig. S10). Therefor, the consumption of H_2O_2 by scavengers was limited, and scavengers were rational to be employed to explore the quenching effects on ROSs. As for the 5.5SACu-*hs*CN/H_2O_2 system (Figs. S9 and 6b-c), with the dosage of TBA varying from 5 to 100 mM, the oxidation efficiency of ACT removal was slowly descended from 91.5% to 61.2% in 180 min, with the corresponding rate constant of *k* dropping from 0.031 to 0.015 min^{-1}. As compared with the original performance of 94.8% and 0.035 min^{-1}, the constantly adding dosage of TBA merely quenched the oxidation to a low extent. It was then inferred that $^{\bullet}$OH was produced in the degradation but not the main ROS. One unanticipated finding was that a slowly adding dose of L-histidine from 0.05 to 2 mM significantly inhibited the oxidation efficiency from 78.4% to 16.7%, accompanied with *k* from 0.019 to a very low value of 0.0057 min^{-1}. In this regard, it was made clear that non-radical of $^1O_2$ was produced and should be the predominant ROS for Fenton-like degradation of ACT. The contributions of $^1O_2$ and $^{\bullet}$OH in 5.5SACu-*hs*CN/H_2O_2 system were further explored (Fig. 6d). As high as 83.3% for $^1O_2$, while only 16.7% for $^{\bullet}$OH was discovered, respectively. It was reported that $^{\bullet}$OH production tended to occur in acid condition, while $^1O_2$ generation was favored in alkaline environment [58]. Additionally, it was just elicited that $^1O_2$ mainly contributed to the ACT degradation rather than $^{\bullet}$OH. These two reasons accounted for the aforementioned results of better efficiencies of ACT degradation at pH of 4–9 than 2–3. With regard to the 5.5AGCu-*hs*CN/H_2O_2 system, the contribution of $^{\bullet}$OH was 74.7%, while as low as 25.3% for $^1O_2$. On account of the above results, in the 5.5SACu-*hs*CN/H_2O_2 system, ROSs of $^{\bullet}$OH and $^1O_2$ were synergistically produced in the Fenton-like reactions. Moreover, contrary to the commonly major working radicals of $^{\bullet}$OH like in the 5.5AGCu-*hs*CN/H_2O_2 system, the $^1O_2$ species played the key role for ACT elimination.

Above study on the catalytic activity revealed that in 5.5SACu-*hs*CN and 5.5AGCu-*hs*CN, the *hs*CN substrate could not stimulate H_2O_2, and Cu species took effect for the H_2O_2 activation and ACT degradation. Besides, considering that the only different property between 5.5SACu-*hs*CN and 5.5AGCu-*hs*CN was the existence of guest Cu, the different

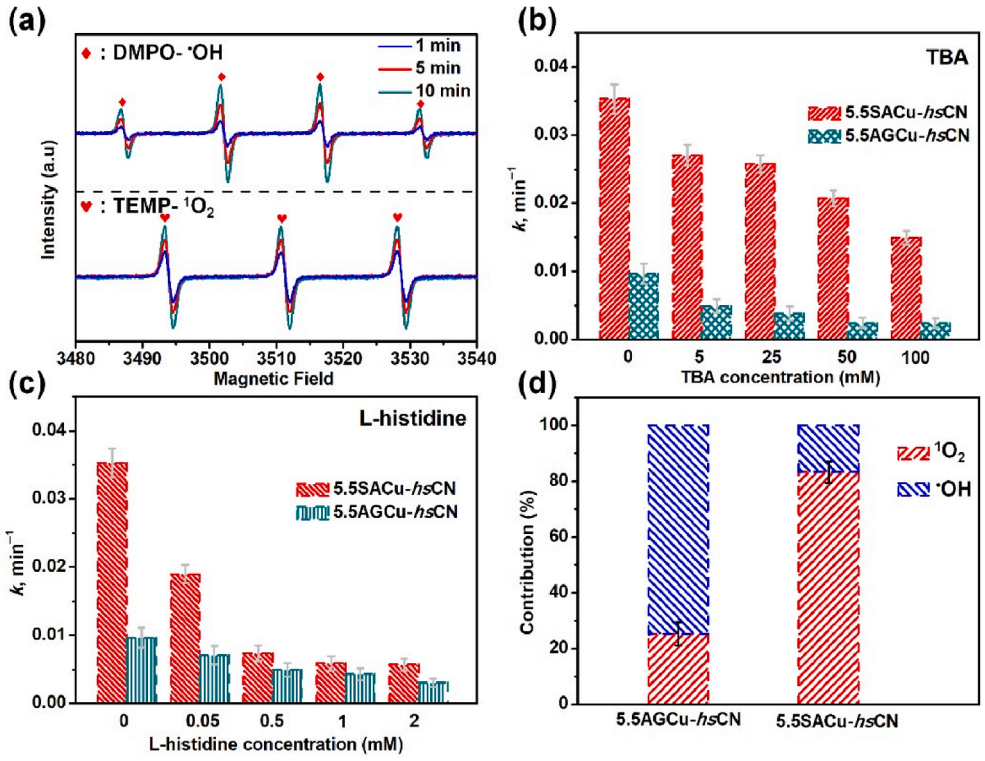

Fig. 6. (a) DMPO and TEMP trapped EPR spectra of the 5.5SACu-*hs*CN/H_2O_2 system; the changes in *k* with the quenching agents of (b) TBA, (c) L-histidine on H_2O_2 activation and ACT removal for the 5.5SACu-*hs*CN, 5.5AGCu-*hs*CN catalyst; (d) the contribution of $^1O_2$ and ·OH radicals. ([Catalyst]$_0$ = 0.2 g·L^{-1}, [H_2O_2]$_0$ = 1000 ppm, [T] = 40 °C, and [ACT]$_0$ = 20 mg·L^{-1}).

major ROSs while interacting with H_2O_2 were thus probably due to the different dispersion behaviors of guest Cu. Single atom Cu-N_3 sites in 5.5SACu-*hs*CN gave rise to the unusual leading role of non-radical $^1O_2$, while aggregated Cu in 5.5AGCu-*hs*CN resulted in the common dominant ·OH radicals. With above results and discussion, single atom Cu-N_3 sites in 5.5SACu-*hs*CN assumed the function of activating H_2O_2, and referring to previous reports [59–61], the mechanism of Fenton-like reactions on ACT oxidation for 5.5SACu-*hs*CN/H_2O_2 system was proposed and shown in Eqs. (2)–(8). The intermediates generated during the transformation of ACT into CO_2 and H_2O were investigated by LC-MS and displayed in Fig. S11.

$$Cu^{+}-N_3+H_2O_2\rightarrow Cu^{2+}-N_3+{}^{\bullet}OH+OH^{-} \quad (2)$$

$$Cu^{2+}-N_3+H_2O_2\rightarrow Cu^{+}-N_3+HO_2^{\bullet}+H^{+} \quad (3)$$

$$H_2O_2+{}^{\bullet}OH\rightarrow H_2O+HO_2^{\bullet} \quad (4)$$

$$Cu^{2+}-N_3+HO_2^{\bullet}\rightarrow Cu^{+}-N_3+{}^1O_2+H^{+} \quad (5)$$

$$HO_2^{\bullet}+HO_2^{\bullet}\rightarrow H_2O_2+{}^1O_2 \quad (6)$$

$${}^{\bullet}OH+HO_2^{\bullet}\rightarrow H_2O+{}^1O_2 \quad (7)$$

$$ACT+ROSs({}^{\bullet}OH+{}^1O_2)\rightarrow intermediates\rightarrow CO_2+H_2O \quad (8)$$

4. Conclusions

This study aims to improve the efficiency in AOPs for removing refractory organic pollutants in water. We demonstrated that the single atom Cu catalyst of 5.5SACu-*hs*CN was successfully fabricated. The atomic Cu-N_3 sites on hollow spherical g-C_3N_4 endowed 5.5SACu-*hs*CN with advantageous Fenton-like activity on the removal of organic pollutants. 94.8% of ACT was degraded within 180 min of catalytic oxidation with *k* of 0.035 min^{-1} by use of 5.5SACu-*hs*CN, which not only outperformed that of 5.5AGCu-*hs*CN loading with aggregated Cu particles with *k* of 0.0097 min^{-1} by 3.6 times (56.7% in 180 min), but also surpassed many reported materials. In addition, the 5.5SACu-*hs*CN/H_2O_2 system took effect over a wide working pH range (4–9), and showed a good durability. Mechanistic investigation revealed that ·OH radicals and non-radical $^1O_2$ jointly served as the reactive oxygen species for ACT elimination in the 5.5SACu-*hs*CN/H_2O_2 system. One unanticipated finding was that, $^1O_2$ was the decisive factor rather than the generally recognized ·OH in Fenton-like reactions. This contribution provides an avenue for promoting the performances of metal based AOP catalysts in the application of wastewater treatment.

CRediT authorship contribution statement

Shuoyuan Tian: Methodology, Investigation, Formal analysis, Visualization, Writing – original draft. **Yu Yin:** Conceptualization, Data curation, Writing – review & editing, Funding acquisition. **Mengxuan Liu:** Methodology, Validation. **Lei Shi:** Validation. **Shu Zhang:** Resources. **Abdul Hannan Asif:** Validation. **Xuan Li:** Investigation. **Mengqiong Liu:** Investigation. **Xiaoguang Duan:** Supervision. **Shaobin Wang:** Supervision. **Hongqi Sun:** Supervision, Project administration, Writing – review & editing.

Declaration of Competing Interest

The authors declare that they have no known competing financial interests or personal relationships that could have appeared to influence the work reported in this paper.

Data availability

Data will be made available on request.

Acknowledgement

The authors greatly appreciate the support provided by the National Natural Science Foundation of China (No. 22278228 and 51602133). The authors also would like to thank Shiyanjia Lab (www.shiyanjia.com) for the aberration corrected HAADF-STEM test.

Appendix A. Supplementary material

Supplementary data to this article can be found online at https://doi.org/10.1016/j.seppur.2023.124016.

References

[1] M. Qutob, M. Rafatullah, M. Qamar, H.S. Alorfi, A.N. Al-Romaizan, M.A. Hussein, A review on heterogeneous oxidation of acetaminophen based on micro and nanoparticles catalyzed by different activators, Nanotechnol. Rev. 11 (2022) 497–525, https://doi.org/10.1515/ntrev-2022-0030.

[2] B. Czech, K. Tyszczuk-Rotko, Visible-light-driven photocatalytic removal of acetaminophen from water using a novel MWCNT-TiO_2-SiO_2 photocatalysts, Sep. Purif. Technol. 206 (2018) 343–355, https://doi.org/10.1016/j.seppur.2018.06.025.

[3] J.L. Peng, Y.L. He, C.Y. Zhou, S.J. Su, B. Lai, The carbon nanotubes-based materials and their applications for organic pollutant removal: A critical review, Chin. Chem. Lett. 32 (2021) 1626–1636, https://doi.org/10.1016/j.cclet.2020.10.026.

[4] M.C. Wen, G.Y. Li, H.L. Liu, J.Y. Chen, T.C. An, H. Yamashita, Metal-organic framework-based nanomaterials for adsorption and photocatalytic degradation of gaseous pollutants: Recent progress and challenges, Environ. Sci. Nano 6 (2019) 1006–1025, https://doi.org/10.1039/c8en01167b.

[5] E. Lipczynska-Kochany, Humic substances, their microbial interactions and effects on biological transformations of organic pollutants in water and soil: A review, Chemosphere 202 (2018) 420–437, https://doi.org/10.1016/j.chemosphere.2018.03.104.

[6] G. Lofrano, S. Meric, G.E. Zengin, D. Orhon, Chemical and biological treatment technologies for leather tannery chemicals and wastewaters: A review, Sci. Total Environ. 461 (2013) 265–281, https://doi.org/10.1016/j.scitotenv.2013.05.004.

[7] D.B. Miklos, C. Remy, M. Jekel, K.G. Linden, J.E. Drewes, U. Hubner, Evaluation of advanced oxidation processes for water and wastewater treatment - a critical review, Water Res. 139 (2018) 118–131, https://doi.org/10.1016/j.watres.2018.03.042.

[8] Y. Yin, H. Wu, L. Shi, J. Zhang, X. Xu, H. Zhang, S. Wang, M. Sillanpää, H. Sun, Quasi single cobalt sites in nanopores for superior catalytic oxidation of organic pollutants, Environ. Sci. Nano 5 (2018) 2842–2852, https://doi.org/10.1039/c8en01047a.

[9] D. Meyerstein, Re-examining Fenton and Fenton-like reactions, Nat. Rev. Chem. 5 (2021) 595–597, https://doi.org/10.1038/s41570-021-00310-4.

[10] Y. Yin, W. Li, C. Xu, L. Shi, L.-C. Zhang, Z. Ao, M. Liu, M. Lu, X. Duan, S. Wang, S. Liu, H. Sun, Ultrafine copper nanoclusters and single sites for Fenton-like reactions with high atom utilities, Environ. Sci. Nano 7 (2020) 2595–2606, https://doi.org/10.1039/d0en00505c.

[11] R. Li, D. Speed, D. Siriwardena, S. Fernando, S.M. Thagard, T.M. Holsen, Comparison of hydrogen peroxide-based advanced oxidation processes for the treatment of azole-containing industrial wastewater, Chem. Eng. J. 425 (2021), 131785, https://doi.org/10.1016/j.cej.2021.131785.

[12] S. Jimenez, M. Andreozzi, M.M. Mico, M.G. Alvarez, S. Contreras, Produced water treatment by advanced oxidation processes, Sci. Total Environ. 666 (2019) 12–21, https://doi.org/10.1016/j.scitotenv.2019.02.128.

[13] M. Xie, M.Y. Yao, S.Y. Zhang, L.S. Kong, L.X. Zhao, J.H. Zhan, R.S. Zhao, Single-atom Co-N_5 catalytic sites on carbon nanotubes as peroxymonosulfate activator for sulfamerazine degradation via enhanced electron transfer pathway, Sep. Purif. Technol. 304 (2023), 122398, https://doi.org/10.1016/j.seppur.2022.122398.

[14] R.Z. Li, D.S. Wang, Understanding the structure-performance relationship of active sites at atomic scale, Nano Res. 15 (2022) 6888–6923, https://doi.org/10.1007/s12274-022-4371-x.

[15] M.K. Samantaray, V. D'Elia, E. Pump, L. Falivene, M. Harb, S. Ould Chikh, L. Cavallo, J.M. Basset, The comparison between single atom catalysis and surface organometallic catalysis, Chem. Rev. 120 (2020) 734–813, https://doi.org/10.1021/acs.chemrev.9b00238.

[16] S. Mitchell, E. Vorobyeva, J. Perez-Ramirez, The multifaceted reactivity of single-atom heterogeneous catalysts, Angew. Chem. Int. Ed. 57 (2018) 15316–15329, https://doi.org/10.1002/anie.201806936.

[17] Z.K. Huang, H.J. Yu, L. Wang, M.Y. Wang, X.W. Liu, D. Shen, S.D. Shen, S.N. Ren, T.F. Lin, S.Y. Lei, Ferrocene doped ZIF-8 derived Fe-N-C single atom catalyst to active peroxymonosulfate for removal of bisphenol A, Sep. Purif. Technol. 305 (2023), 122402, https://doi.org/10.1016/j.seppur.2022.122402.

[18] Y. Xiong, H. Li, C. Liu, L. Zheng, C. Liu, J.O. Wang, S. Liu, Y. Han, L. Gu, J. Qian, D. Wang, Single-atom Fe catalysts for Fenton-like reactions: Roles of different N species, Adv. Mater. 34 (2022) 2110653, https://doi.org/10.1002/adma.202110653.

[19] Y. Yin, L. Shi, W. Li, X. Li, H. Wu, Z. Ao, W. Tian, S. Liu, S. Wang, H. Sun, Boosting Fenton-like reactions via single atom Fe catalysis, Environ. Sci. Technol. 53 (2019) 11391–11400, https://doi.org/10.1021/acs.est.9b03342.

[20] X. Li, X. Huang, S. Xi, S. Miao, J. Ding, W. Cai, S. Liu, X. Yang, H. Yang, J. Gao, J. Wang, Y. Huang, T. Zhang, B. Liu, Single cobalt atoms anchored on porous N-doped graphene with dual reaction sites for efficient Fenton-like catalysis, J. Am. Chem. Soc. 140 (2018) 12469–12475, https://doi.org/10.1021/jacs.8b05992.

[21] Y. Zou, J. Hu, B. Li, L. Lin, Y. Li, F. Liu, X.-Y. Li, Tailoring the coordination environment of cobalt in a single-atom catalyst through phosphorus doping for enhanced activation of peroxymonosulfate and thus efficient degradation of sulfadiazine, Appl. Catal. B 312 (2022), 121408, https://doi.org/10.1016/j.apcatb.2022.121408.

[22] B.Q. Wang, C. Cheng, M.M. Jin, J. He, H. Zhang, W. Ren, J. Li, D.S. Wang, Y.D. Li, A site distance effect induced by reactant molecule matchup in single-atom catalysts for Fenton-like reactions, Angew. Chem. Int. Ed. 61 (2022) e202207268.

[23] Q. Liu, H. Li, H. Zhang, Z. Shen, H. Ji, The role of Cs dopants for improved activation of molecular oxygen and degradation of tetracycline over carbon nitride, Chin. Chem. Lett. 33 (2022) 4756–4760, https://doi.org/10.1016/j.cclet.2021.12.089.

[24] X. Zhao, Q. Liu, X. Li, H. Ji, Z. Shen, Two-dimensional g-C_3N_4 nanosheets-based photo-catalysts for typical sustainable processes, Chin. Chem. Lett. 108306 (2023), https://doi.org/10.1016/j.cclet.2023.108306.

[25] D.D. Yang, Y. Hu, P.D. Hong, G.Q. Shen, Y.L. Li, J.Y. He, K.S. Zhang, Z.J. Wu, C. Xie, J.H. Liu, L.T. Kong, Preassembly strategy to anchor single atoms on carbon nitride layers achieving versatile Fenton-like catalysis, Sep. Purif. Technol. 308 (2023), 122955, https://doi.org/10.1016/j.seppur.2022.122955.

[26] X.Y. Mi, P.F. Wang, S.Z. Xu, L.N. Su, H. Zhong, H.T. Wang, Y. Li, S.H. Zhan, Almost 100 % peroxymonosulfate conversion to singlet oxygen on single-atom CoN_{2+2} sites, Angew. Chem. Int. Ed. 60 (2021) 4588–4593, https://doi.org/10.1002/anie.202014472.

[27] Y. Yin, M. Liu, L. Shi, S. Zhang, R.A.K. Hirani, C. Zhu, C. Chen, A. Yuan, X. Duan, S. Wang, H. Sun, Highly dispersive Ru confined in porous ultrathin g-C_3N_4 nanosheets as an efficient peroxymonosulfate activator for removal of organic pollutants, J. Hazard. Mater. 435 (2022), 128939, https://doi.org/10.1016/j.jhazmat.2022.128939.

[28] X.M. Peng, J.Q. Wu, Z.L. Zhao, X. Wang, H.L. Dai, L. Xu, G.P. Xu, Y. Jian, F.P. Hu, Activation of peroxymonosulfate by single-atom Fe-g-C_3N_4 catalysts for high efficiency degradation of tetracycline via nonradical pathways: Role of high-valent iron-oxo species and Fe-N*x* sites, Chem. Eng. J. 427 (2022), 130803, https://doi.org/10.1016/j.cej.2021.130803.

[29] L.S. Zhang, X.H. Jiang, Z.A. Zhong, L. Tian, Q. Sun, Y.T. Cui, X. Lu, J.P. Zou, S. L. Luo, Carbon nitride supported high-loading Fe single-atom catalyst for activating of peroxymonosulfate to generate $^1O_2$ with 100 % selectivity, Angew. Chem. Int. Ed. 60 (2021) 21751–21755, https://doi.org/10.1002/anie.202109488.

[30] P. Duan, J. Pan, W. Du, Q. Yue, B. Gao, X. Xu, Activation of peroxymonosulfate via mediated electron transfer mechanism on single-atom Fe catalyst for effective organic pollutants removal, Appl. Catal. B 299 (2021) 120714, https://doi.org/10.1016/j.apcatb.2021.120714.

[31] Z. Guo, Y.B. Xie, J.D. Xiao, Z.J. Zhao, Y.X. Wang, Z.M. Xu, Y. Zhang, L.C. Yin, H. B. Cao, J.L. Gong, Single-atom Mn-N_4 site-catalyzed peroxone reaction for the efficient production of hydroxyl radicals in an acidic solution, J. Am. Chem. Soc. 141 (2019) 12005–12010, https://doi.org/10.1021/jacs.9b04569.

[32] F. Guo, Z.H. Chen, X.L. Huang, L.W. Cao, X.F. Cheng, W.L. Shi, L.Z. Chen, Cu_3P nanoparticles decorated hollow tubular carbon nitride as a superior photocatalyst for photodegradation of tetracycline under visible light, Sep. Purif. Technol. 275 (2021), 119223, https://doi.org/10.1016/j.seppur.2021.119223.

[33] M. Tahir, N. Mahmood, X.X. Zhang, T. Mahmood, F.K. Butt, I. Aslam, M. Tanveer, F. Idrees, S. Khalid, I. Shakir, Y.M. Yan, J.J. Zou, C.B. Cao, Y.L. Hou, Bifunctional catalysts of Co_3O_4@GCN tubular nanostructured (TNS) hybrids for oxygen and hydrogen evolution reactions, Nano Res. 8 (2015) 3725–3736, https://doi.org/10.1007/s12274-015-0872-1.

[34] Z. Huang, Y. Zhang, H. Dai, Y. Wang, C. Qin, W. Chen, Y. Zhou, S. Yuan, Highly dispersed Pd nanoparticles hybridizing with 3D hollow-sphere g-C_3N_4 to construct 0D/3D composites for efficient photocatalytic hydrogen evolution, J. Catal. 378 (2019) 331–340, https://doi.org/10.1016/j.jcat.2019.09.007.

[35] Y.S. Jun, E.Z. Lee, X.C. Wang, W.H. Hong, G.D. Stucky, A. Thomas, From melamine-cyanuric acid supramolecular aggregates to carbon nitride hollow spheres, Adv. Funct. Mater. 23 (2013) 3661–3667, https://doi.org/10.1002/adfm.201203732.

[36] Y. Liu, X. Guo, Z. Chen, W. Zhang, Y. Wang, Y. Zheng, X. Tang, M. Zhang, Z. Peng, R. Li, Y. Huang, Microwave-synthesis of g-C_3N_4 nanoribbons assembled seaweed-like architecture with enhanced photocatalytic property, Appl. Catal. B 266 (2020), 118624, https://doi.org/10.1016/j.apcatb.2020.118624.

[37] W. Wang, H. Zhang, S. Zhang, Y. Liu, G. Wang, C. Sun, H. Zhao, Potassium-ion-assisted regeneration of active cyano groups in carbon nitride nanoribbons: Visible-light-driven photocatalytic nitrogen reduction, Angew. Chem. Int. Ed. 58 (2019) 16644–16650, https://doi.org/10.1002/anie.201908640.

[38] Y. Wang, Y. Zhang, J. Yan, J. Yu, B. Ding, One-step synthesis of a macroporous Cu-g/C_3N_4 nanofiber electrocatalyst for efficient oxygen reduction reaction, Chem. Commun. 56 (2020) 14087–14090, https://doi.org/10.1039/D0CC06424F.

[39] D. Adekoya, X.X. Gu, M. Rudge, W. Wen, C. Lai, M. Hankel, S.Q. Zhang, Carbon nitride nanofibres with exceptional lithium storage capacity: From theoretical prediction to experimental implementation, Adv. Funct. Mater. 28 (2018) 1803972, https://doi.org/10.1002/adfm.201803972.

[40] J. Zander, J. Timm, M. Weiss, R. Marschall, Light-induced ammonia generation over defective carbon nitride modified with pyrite, Adv. Energy Mater. 12 (2022) 2202403, https://doi.org/10.1002/aenm.202202403.

[41] S. An, G. Zhang, T. Wang, W. Zhang, K. Li, C. Song, J.T. Miller, S. Miao, J. Wang, X. Guo, High-density ultra-small clusters and single-atom Fe sites embedded in

graphitic carbon nitride (g-C_3N_4) for highly efficient catalytic advanced oxidation processes, ACS Nano 12 (2018) 9441–9450, https://doi.org/10.1021/acsnano.8b04693.
[42] X. Mi, H. Zhong, H. Zhang, S. Xu, Y. Li, H. Wang, S. Zhan, J.C. Crittenden, Facilitating redox cycles of copper species by pollutants in peroxymonosulfate activation, Environ. Sci. Technol. 56 (2022) 2637–2646, https://doi.org/10.1021/acs.est.1c06762.
[43] X. Qian, X. Meng, J. Sun, L. Jiang, Y. Wang, J. Zhang, X. Hu, M. Shalom, J. Zhu, Salt-assisted synthesis of 3D porous g-C_3N_4 as a bifunctional photo- and electrocatalyst, ACS Appl. Mater. Interfaces 11 (2019) 27226–27232, https://doi.org/10.1021/acsami.9b08651.
[44] X. Li, G. Dong, F. Guo, P. Zhu, Y. Huang, C. Wang, Enhancement of photocatalytic no removal activity of g-C_3N_4 by modification with illite particles, Environ. Sci. Nano 7 (2020) 1990–1998, https://doi.org/10.1039/d0en00415d.
[45] M. Zhang, Y. Yang, X. An, J. Zhao, Y. Bao, L.A. Hou, Exfoliation method matters: The microstructure-dependent photoactivity of g-C_3N_4 nanosheets for water purification, J. Hazard. Mater. 424 (2022), 127424, https://doi.org/10.1016/j.jhazmat.2021.127424.
[46] R.-C. Wang, Y.-C. Lin, H.-C. Chen, W.-Y. Lin, Energy harvesting from g-C_3N_4 piezoelectric nanogenerators, Nano Energy 83 (2021), 105743, https://doi.org/10.1016/j.nanoen.2021.105743.
[47] T. Zhang, D. Zhang, X. Han, T. Dong, X. Guo, C. Song, R. Si, W. Liu, Y. Liu, Z. Zhao, Preassembly strategy to fabricate porous hollow carbonitride spheres inlaid with single Cu-N_3 sites for selective oxidation of benzene to phenol, J. Am. Chem. Soc. 140 (2018) 16936–16940, https://doi.org/10.1021/jacs.8b10703.
[48] G. Wang, T. Zhang, W. Yu, R. Si, Y. Liu, Z. Zhao, Modulating location of single copper atoms in polymeric carbon nitride for enhanced photoredox catalysis, ACS Catal. 10 (2020) 5715–5722, https://doi.org/10.1021/acscatal.0c01099.
[49] Y.T. Qu, Z.J. Li, W.X. Chen, Y. Lin, T.W. Yuan, Z.K. Yang, C.M. Zhao, J. Wang, C. Zhao, X. Wang, F.Y. Zhou, Z.B. Zhuang, Y. Wu, Y.D. Li, Direct transformation of bulk copper into copper single sites via emitting and trapping of atoms, Nat. Catal. 1 (2018) 781–786, https://doi.org/10.1038/s41929-018-0146-x.
[50] F. Li, Z. Lu, T. Li, P. Zhang, C. Hu, Origin of the excellent activity and selectivity of a single-atom copper catalyst with unsaturated Cu-N_2 sites via peroxydisulfate activation: Cu(III) as a dominant oxidizing species, Environ. Sci. Technol. 56 (2022) 8765–8775, https://doi.org/10.1021/acs.est.2c00369.
[51] X.D. Xiao, Y.T. Gao, L.P. Zhang, J.C. Zhang, Q. Zhang, Q. Li, H.L. Bao, J. Zhou, S. Miao, N. Chen, J.Q. Wang, B.J. Jiang, C.G. Tian, H.G. Fu, A promoted charge separation/transfer system from Cu single atoms and C_3N_4 layers for efficient photocatalysis, Adv. Mater. 32 (2020) 2003082, https://doi.org/10.1002/adma.202003082.
[52] H.S. Shang, X.Y. Zhou, J.C. Dong, A. Li, X. Zhao, Q.H. Liu, Y. Lin, J.J. Pei, Z. Li, Z. L. Jiang, D.N. Zhou, L.R. Zheng, Y. Wang, J. Zhou, Z.K. Yang, R. Cao, R. Sarangi, T. T. Sun, X. Yang, X.S. Zheng, W.S. Yan, Z.B. Zhuang, J. Li, W.X. Chen, D.S. Wang, J. T. Zhang, Y.D. Li, Engineering unsymmetrically coordinated Cu-S_1N_3 single atom sites with enhanced oxygen reduction activity, Nat. Commun. 11 (2020) 3049, https://doi.org/10.1038/s41467-020-16848-8.
[53] Y. Li, B.H. Li, D.N. Zhang, L. Cheng, Q.J. Xiang, Crystalline carbon nitride supported copper single atoms for photocatalytic CO_2 reduction with nearly 100% CO selectivity, ACS Nano 14 (2020) 10552–10561, https://doi.org/10.1021/acsnano.0c04544.
[54] L.M. Jin, S.J. You, Y. Yao, H. Chen, Y. Wang, Y.B.A. Liu, An electroactive single-atom copper anchored MXene nanohybrid filter for ultrafast water decontamination, J. Mater. Chem. A 9 (2021) 25964–25973, https://doi.org/10.1039/d1ta07396f.
[55] H. Li, S. Sun, H. Ji, W. Liu, Z. Shen, Enhanced activation of molecular oxygen and degradation of tetracycline over Cu-S4 atomic clusters, Appl. Catal., B 272 (2020) 118966, https://doi.org/10.1016/j.apcatb.2020.118966.
[56] Y. Yang, G. Banerjee, G.W. Brudvig, J.H. Kim, J.J. Pignatello, Oxidation of organic compounds in water by unactivated peroxymonosulfate, Environ. Sci. Technol. 52 (2018) 5911–5919, https://doi.org/10.1021/acs.est.8b00735.
[57] C. Zhu, S. Zhao, Z. Fan, H. Wu, F. Liu, Z. Chen, A. Li, Confinement of CoP nanoparticles in nitrogen-doped yolk-shell porous carbon polyhedron for ultrafast catalytic oxidation, Adv. Funct. Mater. 30 (2020) 2003947, https://doi.org/10.1002/adfm.202003947.
[58] J. Lim, H. Kim, J. Park, G.-H. Moon, J.J.M. Vequizo, A. Yamakata, J. Lee, W. Choi, How g-C_3N_4 works and is different from TiO_2 as an environmental photocatalyst: Mechanistic view, Environ. Sci. Technol. 54 (2020) 497–506, https://doi.org/10.1021/acs.est.9b05044.
[59] Z. Huang, M. Shen, J. Liu, J. Ye, T. Asefa, Facile synthesis of an effective g-C_3N_4-based catalyst for advanced oxidation processes and degradation of organic compounds, J. Mater. Chem. A 9 (2021) 14841–14850, https://doi.org/10.1039/d1ta01325d.
[60] Z. Yang, J. Qian, A. Yu, B. Pan, Singlet oxygen mediated iron-based Fenton-like catalysis under nanoconfinement, Proc. Natl. Acad. Sci. USA 116 (2019) 6659–6664, https://doi.org/10.1073/pnas.1819382116.
[61] R. Yamaguchi, S. Kurosu, M. Suzuki, Y. Kawase, Hydroxyl radical generation by zero-valent iron/Cu (ZVI/Cu) bimetallic catalyst in wastewater treatment: Heterogeneous Fenton/Fenton-like reactions by Fenton reagents formed in-situ under oxic conditions, Chem. Eng. J. 334 (2018) 1537–1549, https://doi.org/10.1016/j.cej.2017.10.154.